Supporting Information

Engineering the Electronic States of Ni₃FeN via Zinc Ions Regulating for Promoted Oxygen Electrocatalysis in Rechargeable Zn-air Batteries

Xiaoyang He[a], Yuhui Tian[a,d], Zengliang Huang[a], Li Xu[a,*], Jianchun Wu[a,c], Junchao Qian[b], Jianming Zhang[a], Henan Li[a,*]

[a.] *Institute for Energy Research, School of Chemistry and Chemical Engineering, School of Materials Science and Engineering, Key Laboratory of Zhenjiang, Jiangsu University, Zhenjiang 212013, P. R. China. E-mail: xulichem@ujs.edu.cn; lhn@ujs.edu.cn.*

[b.] *Jiangsu Key Laboratory for Environment Functional Materials, Suzhou University of Science and Technology, Suzhou 215009, P. R. China.*

[c] *Institute of Nuclear Science and Technology, Sichuan University, Chengdu, 610064, P. R. China.*

[d] *Centre for Clean Environment and Energy, Griffith School of Environment, Gold Coast Campus, Griffith University, QLD 4222, Australia.*

Experimental details

Chemical.

Urea ($CO(NH_2)_2$), 99%, ferric(III) nitrate nonahydrate ($Fe(NO_3)_3 \cdot 9H_2O$, 99%), nickel(II) nitrate hexahydrate ($Ni(NO_3)_2 \cdot 6H_2O$, 99%), zinc(II) nitrate hexahydrate($Zn(NO_3)_2 \cdot 6H_2O$), hydrochloric acid (HCl, 36%) and ethanol (C_2H_5OH, 99.7%) were obtained from Sino Pharm Chemical Reagent Co., Ltd (Shanghai, China). Commercial Pt/C (20 wt% Pt/C) and RuO_2 were procured from Alfa Aesar (China) Chemicals Co. Ltd (Shanghai). Nafion (10 wt%) was purchased from Sigma-Aldrich Chemie Gmbh (Shanghai, China). Reduced graphene oxide was purchased from Nanjing XFNANO Materials Tech Co., Ltd (Nanjing, China).

Synthesis of the Zn-Ni₃FeN/NG.

First, the $g\text{-}C_3N_4$ was synthesized via a simple annealing process. The $g\text{-}C_3N_4$ was synthesized by carbonization urea at 250 °C for 2 h followed by a subsequent thermal treatment at 600 °C for 2 h with a temperature ramping rate of 1 °C min^{-1} in N_2 atmosphere. In a typical experiment, 0.6 mmol nickel nitrate hexahydrate, 0.2 mmol ferric nitrate nonahydrate, 0.1 mmol zinc nitrate hexahydrate, and 6 mmol urea were dissolved in 20 ml deionized water, then mixed with 20 ml aqueous solution containing 20 mg reduced graphene oxide and 0.2 g $g\text{-}C_3N_4$, the mixture was under vigorous magnetic stirring to form a hydrogel. The resultant mixture was then transferred to a Teflon-lined steel autoclave and heated at 120 °C for 18 h in an oven. The precipitates were collected by centrifugation and washed with deionized water and ethanol several times, then centrifuged and dried in a vacuum oven at 60 °C. The dried solid was firstly transferred into a quartz tube with a closed one-terminal. Then the other end of the quartz tube was installed with a mating flange. The vacuum pump was then utilized to remove the internal air from the quartz tube. Next, the quartz tube was transferred into a small muffle furnace (KSL-1100X-S) that had been heated to 850 °C. After 10 min, the heated quartz furnace was immediately taken out of the small muffle furnace and placed in a fume hood. After cooling down to room temperature, the calcined black sample was taken out of the quartz tube and then dispersed in an H_2SO_4 solution (0.5 mol L^{-1}). After being continuously stirred for 12 h, the above sample was washed until neutral with deionized water, and then dried at 60 °C. The Zn-Ni₃Fe alloys/nitrogen-doped graphene (Zn-Ni₃Fe/NG) was obtained (Fig. S1). Finally, to obtain the Zn-doped Ni₃FeN/NG, the dried sample was placed in a tube furnace and annealed at 800 °C for 1.5 h in NH_3 at a heating rate of 5 °C min^{-1}. After natural cooling to room temperature, the Zn-Ni₃FeN/NG was collected.

Synthesis of the Zn-Ni₄N/NG.

The Zn-Ni₄N/NG was prepared through the same process as that of Zn-Ni₃FeN/NG except that Fe source was not added to the reaction system and the amount of nickel nitrate hexahydrate was changed to 0.8 mmol.

Synthesis of the Zn-FeN/NG.

The Zn-FeN/NG was prepared through the same process as that of Zn-Ni₃FeN/NG except that Ni source was not added to the reaction system and the amount of ferric nitrate nonahydrate was changed to 0.8 mmol.

Synthesis of the Ni$_3$FeN/NG.

The Ni$_3$FeN/NG was prepared through the same process as that of Zn-Ni$_3$FeN/NG except that Zn source was not added to the reaction system and the amount of ferric nitrate hexahydrate and nickel nitrate hexahydrate was changed to 0.65, 0.25 mmol, respectively.

Characterizations.

The phase purity and crystalline phases of all samples were characterized by X-ray diffraction (XRD, Bruker D8 diffractometer) with Cu Ka radiation (λ = 1.5418 Å) in 2 theta range of 10-80°. The form of the elements on the surface of Zn-Ni$_3$FeN/NG was explored by X-ray photoelectron spectroscopy (XPS, ESCALAB 250xl, Thermo VG Scientific, USA) at 1 kV. The field-emission scanning electron microscopy (FE-SEM) images with a field-emission scanning electron microscope (JEOL JSM-7800F) were recorded. Transmission electron microscopy (TEM, JEOL JEM-2010) images and energy-dispersive X-ray (EDX) mapping measurements were measured to research the morphologies of the synthesized materials. The specific surface areas of as-prepared electrocatalysts were confirmed by Brunauer-Emmett-Teller (BET, Tristar 3020).

Electrochemical measurement.

Electrocatalytic properties of all synthesized materials were investigated on CHI 760E (CHI Shanghai, Inc.) electrochemical workstation with a traditional three-electrode system. The reference electrode was an Ag/AgCl immersed in a saturated KCl solution. A graphite rod was utilized as the counter electrode. The working electrodes were rotating disk electrodes (RDE, diameter = 3 mm) and rotating ring-disk electrode (RRDE, the diameter of glassy carbon = 4 mm, and diameter of platinum ring = 7 mm) modified by as-prepared electrocatalysts. The modification of the working electrodes was as follows: 5 mg of sample was ultrasonically dispersed in a mixture of 500 uL ethanol, 500 uL deionized water, and 20 uL 10 wt% Nafion to obtain the slurry. 7.5 and 10 uL slurries were then dropwise added onto cleaned RDE and RRDE, and then dried at room temperature, respectively. In contrast, electrodes modified by 20 wt% Pt/C were prepared with the same method.

The electrolyte was KOH (0.1 mol L^{-1}) in the test system. All potentials were converted to reversible hydrogen electrodes (RHE). The electron transfer number (n) and hydrogen peroxide($H{O_2}^-$) yield of Zn-Ni$_3$FeN/NG and 20 wt% Pt/C during ORR were measured by RRDE electrodes and calculated by Eq.(1) and (2). The ring potential was kept at 0.286 V. N is the collection coefficient of $H{O_2}^-$ with a value of 0.37 in Eq.(1) and (2). I_d and I_r represent the disk current and the ring current, respectively.

$$n = 4\, I_d\, /\, (I_d + I_r\, /\, N) \qquad (1)$$

$$HO_2^- = 200(I_r\, /\, N)/(I_d + I_r\, /\, N) \qquad (2)$$

At the rotating speed of 1600 rpm, the stability of Zn-Ni$_3$FeN/NG and 20 wt% Pt/C were elevated for up to 10 h by the current-time(i-t) chronoamperometric response tests with the rotation speed of 1600 rpm and a sweep rate of 10 mV s^{-1} in 0.1 mol L^{-1} O$_2$-saturated KOH.

The OER tests were carried out by using a similar method as ORR. The same amount of catalysts was loaded on the rotating disk working electrode. LSV curves were reordered at the rotating speed of 1600 rpm in N_2-saturated 0.1 M KOH. The data was iR corrected using the iR-drop compensation feature of CHI 760E workstation while conducting the measurements. The Tafel slopes were calculated according to the Tafel Eq. (3) based on the LSV curves.

$$\eta = b \log (j / j_0) \qquad (3)$$

where η is the potential, b is the Tafel slope, j is the current density, and j_0 is the exchange current density.

In order to estimate the electrochemical active surface area (ECSA) of the catalytic surface through RDE, the electrochemical double layer capacitances (C_{dl}) in the non-Faradaic potential region were obtained by Eq.(4) derived from changing CV curves at the scan rate range between 2,5,10,15,20,25 and 50 mV s^{-1}.

$$ECSA = C_{dl}/C_s \qquad (4)$$

Where $C_{dl} = IC/v$. IC is the sum of charging/discharging at 1.0 V (vs. RHE) from different CV curves. V represents the scan rate. C_s is the capacitance of electrocatalytic materials on the smooth surface in the same electrolyte or specific capacitance of the catalysts.

The mass activity was calculated using Eq.(5); the specific activity was calculated using Eq.(6). J_k was calculated using Eq.(7).

$$M = J_k^{@0.85V}/loading_{cat} \qquad (5)$$
$$S = J_k^{@0.85V}/(ECSA*loading_{cat}) \qquad (6)$$
$$J_k^{@0.85V} = (J_d * J^{@0.85V})/(J_d - J^{@0.85V}) \qquad (7)$$

where J_k is the ORR kinetic current, J_d is the limit current.

Liquid Zn-air battery measurement.

To assemble Zn-air batteries, the slurry of Zn-Ni$_3$FeN/NG was dropwise added onto a carbon cloth with an area of 1 cm^{-2} to ensure a loading amount of 1 mg cm^{-2} as the air cathode. The polished Zn plate was used as the anode. The mixed solution of 6 mol L^{-1} KOH and 0.2 mol L^{-1} Zn(CH$_3$COO)$_2$ was the electrolyte solution. The charging and discharging polarization curves were measured by LSV polarization curves with a scan rate of 10 mV s^{-1} and calculated the power density by Eq.(8):

$$power\ density = current\ density \times voltage \qquad (8)$$

The galvanostatic (20 mA cm^{-2}) discharging curve was measured and calculated the specific capacity by Eq. (9):

$$specific\ capacity = (current \times test\ hours)/(consumed\ Zn\ plate\ mass) \qquad (9)$$

The charge-discharge cycle stability was tested with a cycle period of 20 min (10 min for charging and 10 min for discharging).
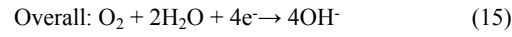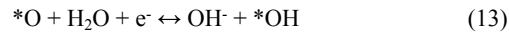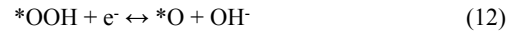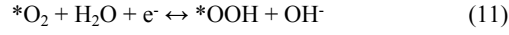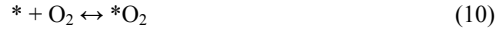
In contrast, the mixture slurry of RuO$_2$ and 20 wt% Pt/C with a mass ratio of 1:1 was dropwise added onto a carbon cloth with an area of 1 cm^{-2} to ensure a loading amount of 1 mg cm^{-2} as the air cathode. It was also used to assemble the Zn-air battery and performed the practical application at the same conditions.

DFT calculations

The computational calculations were carried out using density function theory (DFT) in Vienna ab-initio simulation package (VASP). The generalized gradient approximation (GGA) in the form of the Perdew-Burke-Ernzerhof (PBF)

was used to treat the exchange-correlation function. A kinetic energy cut-off of 400 eV was used for plane-wave expansion. The Brillouin zone was sampled with a 4×4×1 Gamma centered special k-points grid for geometry optimization. All models were established with cell dimension of 7.53 Å×10.65 Å×20 Å, with a vacuum slab of 20 Å in c direction to avoid the artificial interactions between the periodic images. A convergence criterion for the electronic self-consistent loop of $1×10^{-5}$ eV for structure optimization. All the models were geometrically optimized prior to gain all the atoms sitting at the minimum energy point.

The four-electron ORR mechanism in alkaline medium can be summarized as follows:

$$* + O_2 \leftrightarrow *O_2 \tag{10}$$

$$*O_2 + H_2O + e^- \leftrightarrow *OOH + OH^- \tag{11}$$

$$*OOH + e^- \leftrightarrow *O + OH^- \tag{12}$$

$$*O + H_2O + e^- \leftrightarrow OH^- + *OH \tag{13}$$

$$*OH + e^- \leftrightarrow * + OH^- \tag{14}$$

$$\text{Overall: } O_2 + 2H_2O + 4e^- \rightarrow 4OH^- \tag{15}$$

where * represents an active site on the lattice surface. The adsorption energy (ΔE_{ads}) for ORR was calculated as Eq.(16). The adsorption free energy (ΔG_{ads}) is obtained by Eq.(17).

$$E_{ads} = E_{substrate + adsorbate} - E_{substrate} - E_{adsorbate} \tag{16}$$

$$\Delta G = \Delta E + \Delta ZPE - T \cdot \Delta S \tag{17}$$

where ΔE is the energy difference of reactants and products, obtained from DFT calculations; ΔZPE and ΔS are the contributions to the free energy from the zero-point vibration energy and entropy, respectively. T is the temperature (298.15K). And the overpotential is defined as the difference between the potential mentioned above and equilibrium potential (1.23 V) in ORR, described as:

$$\eta = \max[\Delta G1, \Delta G2, \Delta G3, \Delta G4]/e + 1.23V \tag{18}$$
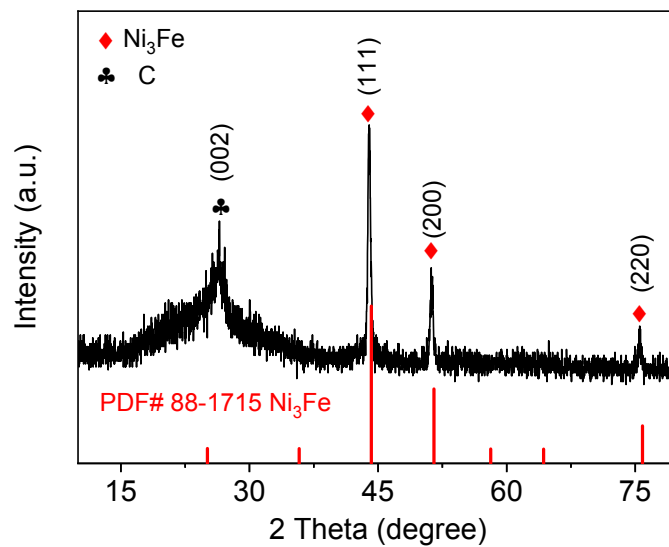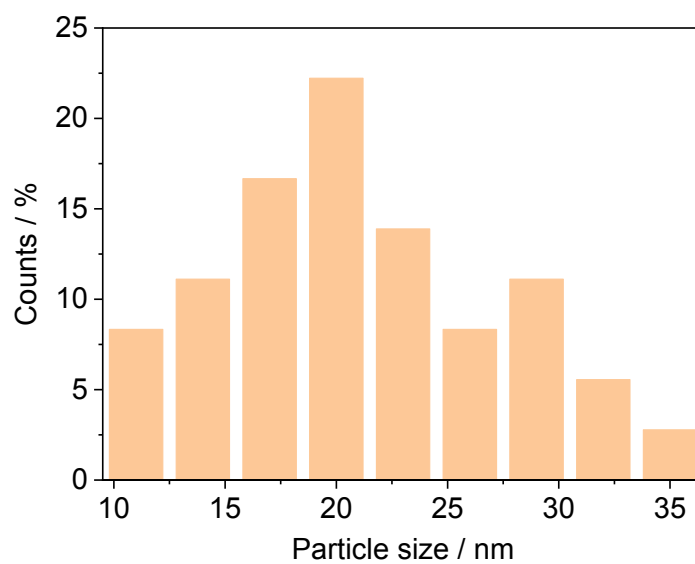
Fig. S1 XRD pattern of the Ni$_3$Fe.

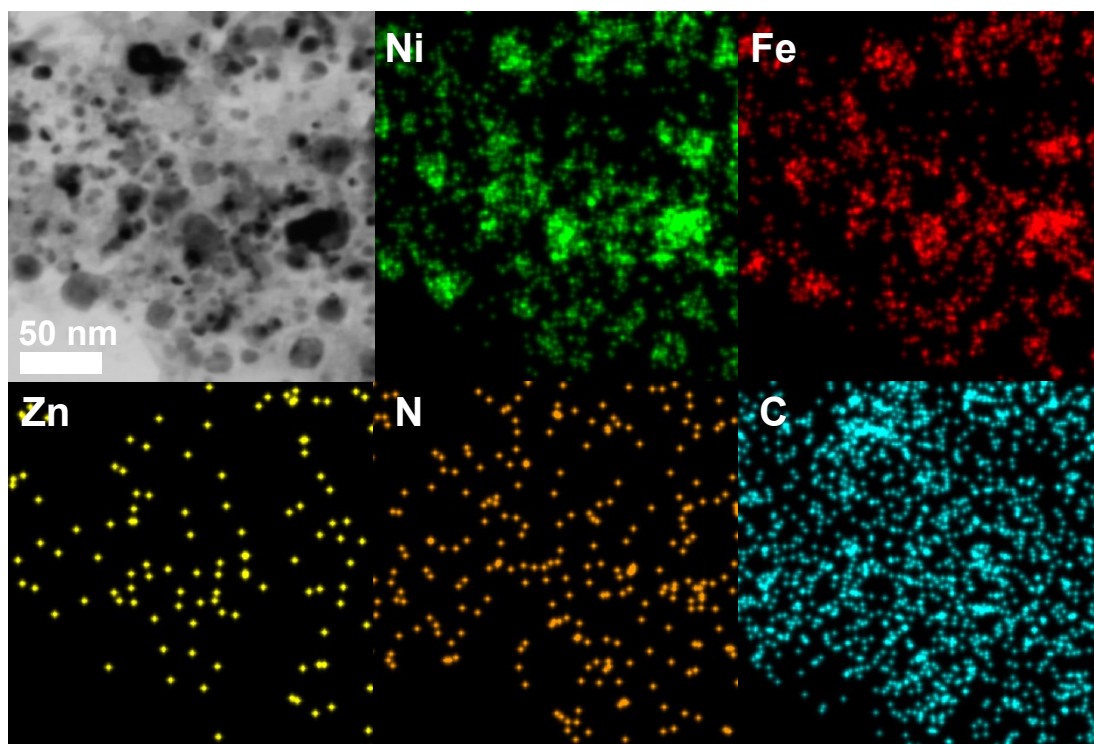Fig. S2 Size histogram of particle diameters of Zn-Ni$_3$FeN/NG.

Fig. S3 TEM image and corresponding EDX mapping images of Zn-Ni$_3$FeN/NG for Ni, Fe, Zn, N, and C.

Fig. S4 (a) XPS survey spectrum of the Zn-Ni$_3$FeN/NG, XPS spectra of (b) C 1s and (c) O 1s elemental in the Zn-Ni$_3$FeN/NG samples.

Fig. S5 N$_2$ adsorption and desorption isotherm curve and pore size distribution plots of (a), (b) Zn-N$_3$FeN/NG; (c), (d) Zn-Ni$_4$N/NG; (e), (f) Zn-FeN/NG and (g), (h) N$_3$FeN/NG.

Fig. S6 (a) RRDE voltammograms of Zn-Ni$_3$FeN/NG and Pt/C in O$_2$-saturated 0.1 M KOH, (b) H$_2$O$_2$% obtained by RRDE technique for Zn-Ni$_3$FeN/NG and Pt/C, and corresponding average electron transfer number (*n*).
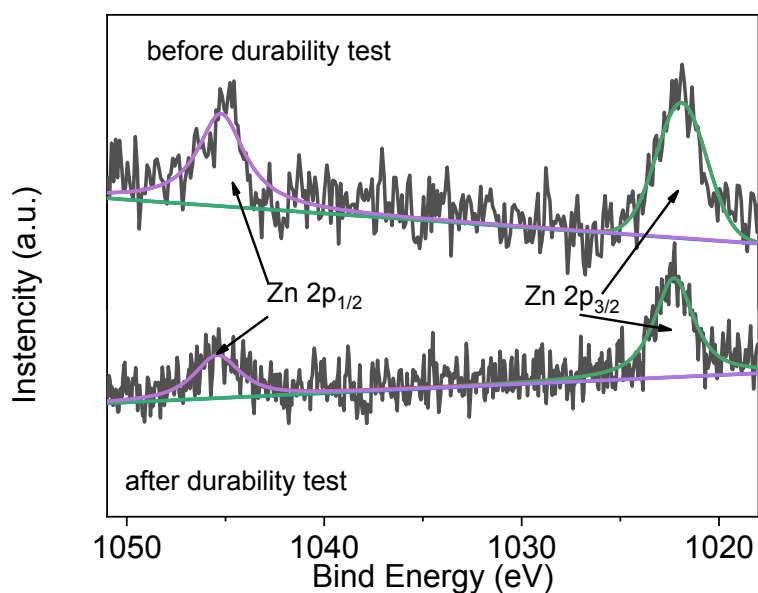

Fig. S7. XPS spectrum of Zn 2p before and after durability testing in the Zn-Ni$_3$FeN/NG.
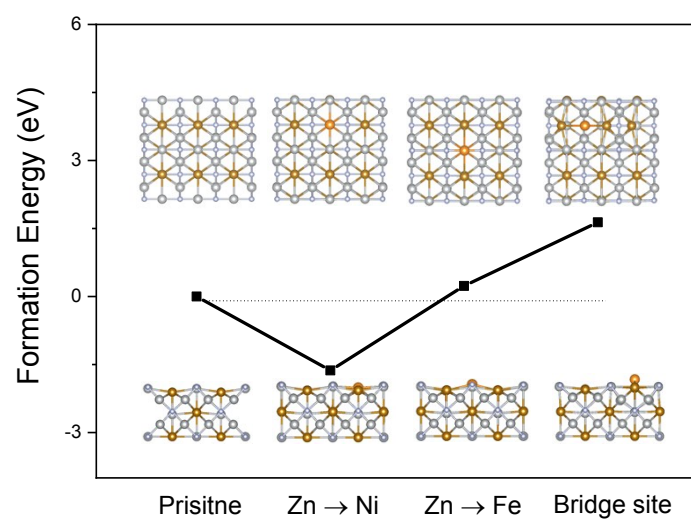
Fig. S8 The formation energy for pristine, a Zn atom replaces a Ni atom (Zn → Ni), a Zn atom replaces a Fe atom (Zn → Fe), Zn atom at the bridge site of two Fe atoms (Bridge site) of Ni_3FeN, respectively.
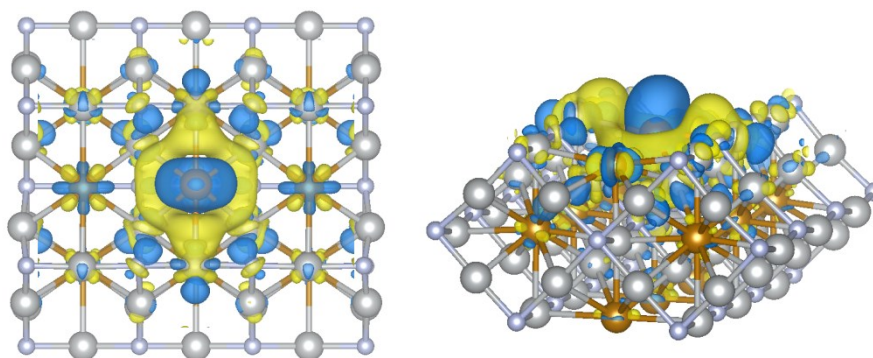

Fig. S9 Schematic illustration of the electron density difference of the Zn-doped Ni_3FeN.
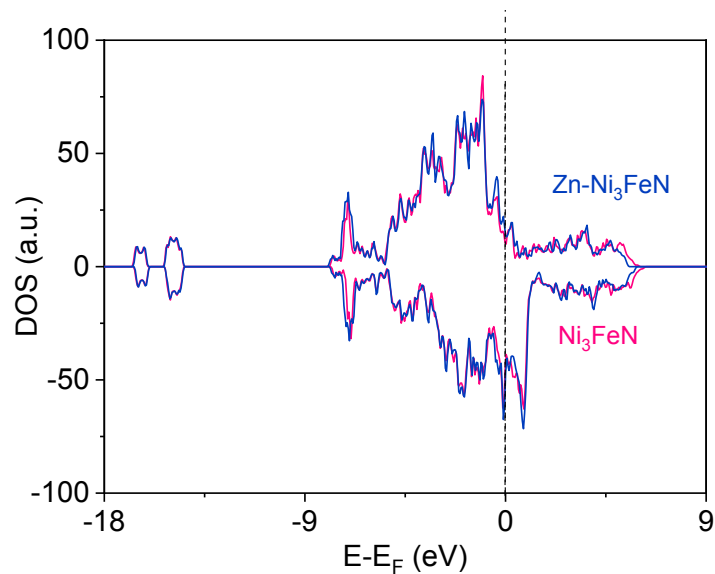
Fig. S10 Total density of states (DOS) of Zn-Ni$_3$FeN and Ni$_3$FeN. The Fermi level is set to zero.

Fig. S11 CVs in the region of 0.96 to 1.06 V vs. RHE at various scan rates and the corresponding linear fitting of the capacitive currents vs. scan rates to estimate the C_{dl}: (a), (b) Zn-N$_3$FeN/NG; (c), (d) Zn-Ni$_4$N/NG; (e), (f) Zn-FeN/NG; (g), (h) N$_3$FeN/NG.
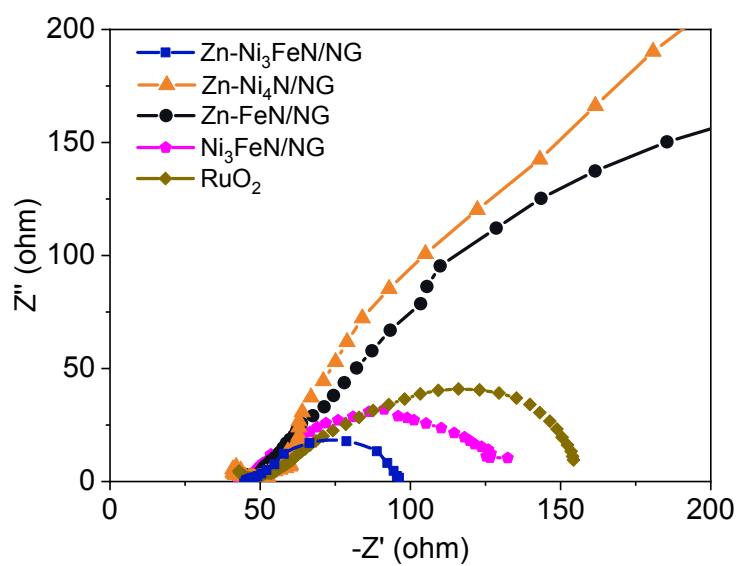

10

Fig. S12 Nyquist plots of Zn-N$_3$FeN/NG, Ni$_3$FeN/NG, Zn-Ni$_4$N/NG, Zn-FeN/NG, and RuO$_2$ in 0.1 M KOH at 1.6 V (vs. RHE).
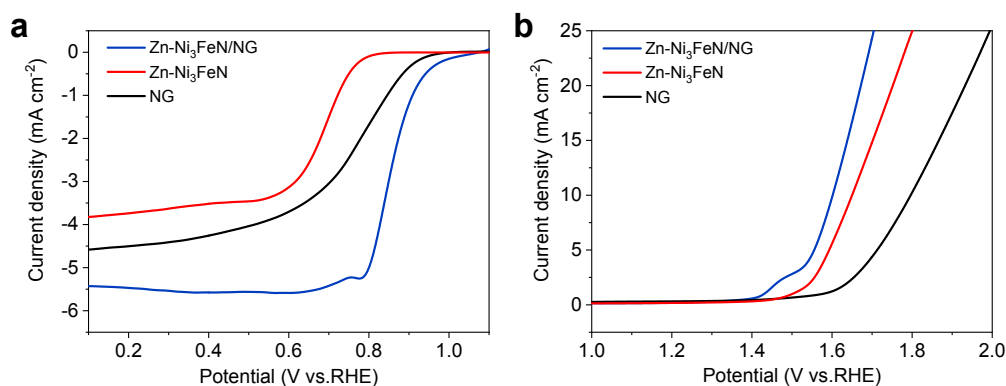
Fig S13. LSV curves for (a) ORR and (b) OER for Zn-Ni$_3$FeN/NG, Zn-Ni$_3$FeN, and NG.

Table S1 Specific surface areas and pore structures of the samples.

Samples	S_{BET} (m^2·g^{-1})	V_p (cm^3·g^{-1})	d (nm)
Zn-Ni$_3$FeN/NG	778.33	2.20	4.048
Zn-Ni$_4$N/NG	291.06	1.05	3.958
Zn-FeN/NG	175.29	0.44	4.022
Ni$_3$FeN/NG	261.85	0.7182	4.130

Table S2 Details of ORR free energy calculation.

△G for each step (eV)	△G1	△G2	△G3	△G4	η
Ni$_3$FeN	-1.747	-1.736	-1.025	-0.412	0.818
Zn-Ni$_3$FeN	-0.543	-0.479	-3.211	-1.687	0.751

Table S3 Comparison of electrocatalytic activity of the Ni$_3$FeN/NG with highly active ORR/OER bifunctional oxygen electrode materials.

Catalyst	$E_{1/2}$ (V)	$E_{j=10}$ (V)	$\triangle E$ / V	Ref.
Zn-Ni$_3$FeN/NG	0.86	1.60	0.74	This work
FeCo/FeCoNi@NCNTs-HF	0.85	1.60	0.75	[1]
FeCo-NC	0.86	1.67	0.81	[2]
Fe$_3$C@Fe,N,S-GCM	0.80	1.55	0.75	[3]
MnCo$_2$O$_4$@C	0.80	1.69	0.89	[4]
CoCoW$_{12}$/NCP	0.81	1.58	0.78	[5]
ZIF-9_Fe3_Pyrol	0.81	1.62	0.81	[6]
Ag-MnO$_2$	0.77	1.58	0.81	[7]
CoA@CNC	0.84	1.69	0.85	[8]
GNCNTs	0.85	1.60	0.75	[9]
Co$_9$S$_8$/N,P-QPC	0.78	1.59	0.81	[10]
N-NiO	0.69	1.50	0.81	[11]
Co$_4$N@NC-m	0.87	1.63	0.76	[12]
Co-Co$_3$O$_4$@NAC	0.79	1.61	0.82	[13]
Co$_{5.47}$N@N-rGO	0.94	1.81	0.77	[14]

Table S4 Comparison of the Zn-air battery performance of Zn-Ni$_3$FeN/NG with highly active ORR/OER bifunctional oxygen electrode materials.

Sample	Power density (mW cm^{-2})	Specific capacity (mAh g^{-1})	cycling performance (h, 10 mA cm^{-2})	Ref.
Zn-Ni$_3$FeN/NG	158	650	180	This work
Fe$_3$O$_4$@NHCS	133	701	50	[15]
LSMF	105	-	15.6	[16]
Co$_4$N@NC	98.6	644	200	[17]
FeNiP/NPCS	163	602	110	[18]
Co-NCF	134	766	50	[19]
N-GQDs/NiCo$_2$S$_4$/CC	75.2	-	200	[20]
CoIn$_2$Se$_4$	107	733	27	[21]
CoP/NC	114	695	35	[22]

Reference

1. Z. Wang, J. Ang, B. Zhang, Y. Zhang, X. Y. D. Ma, T. Yan, J. Liu, B. Che, Y. Huang and X. Lu, *Appl. Catal. B-Environ.*, 2019, **254**, 26-36.

2. G. Li, K. Zheng and C. Xu, *Appl. Surf. Sci.*, 2019, **487**, 496-502.

3. Z. Y. Li, Q. M. Gao, X. Liang, H. Zhang, H. Xiao, P. Xu and Z. P. Liu, *Carbon*, 2019, **150**, 93-100.

4. S. Cui, L. Sun, F. Kong, L. Huo and H. Zhao, *J. Power Sources*, 2019, **430**, 25-31.

5. Y. Wang, X. Xu, J. Chen and Q. Wang, *J. Power Sources*, 2019, **430**, 201-209.

6. F. Kong, Y. Qiao, C. Zhang, R. Li, T. Cheng, A. Kong and Y. Shan, *Catal. Sci. Technolo.*, 2019, **9**, 3469-3481.

7. S. Ni, H. Zhang, Y. Zhao, X. Li, Y. Sun, J. Qian, Q. Xu, P. Gao, D. Wu, K. Kato, M. Yamauchi and Y. Sun, *Chem. Eng. J.*, 2019, **366**, 631-638.

8. M. Shen, K. Gao, F. Xiang, B. Wang, L. Dai, L. Zheng, F. Baker, C. Duan, Y. Zhang, S. Sun and Y. Ni, *J. Power Sources*, 2020, **450**, 227640.

9. Y. Xu, P. Deng, G. Chen, J. Chen, Y. Yan, K. Qi, H. Liu and B. Y. Xia, *Adv. Funct. Mater.*, 2019, **30**, 1906081.

10. X. Hu, Y. Chen, M. Zhang, G. Fu, D. Sun, J.-M. Lee and Y. Tang, *Carbon*, 2019, **144**, 557-566.

11. J. Qian, X. Bai, S. Xi, W. Xiao, D. Gao and J. Wang, *ACS Appl. Mater. Interfaces*, 2019, **11**, 30865-30871.

12. L. Chen, Y. Zhang, X. Liu, L. Long, S. Wang, X. Xu, M. Liu, W. Yang and J. Jia, *Carbon*, 2019, **151**, 10-17.

13. X. Zhong, W. Yi, Y. Qu, L. Zhang, H. Bai, Y. Zhu, J. Wan, S. Chen, M. Yang, L. Huang, M. Gu, H. Pan and B. Xu, *Appl. Catal. B-Environ.*, 2020, **260**, 118188.

14. X. Shu, S. Chen, S. Chen, W. Pan and J. Zhang, *Carbon*, 2020, **157**, 234-243.

15. Y. Li, H. Huang, S. Chen, X. Yu, C. Wang and T. Ma, *Nano Res.*, 2019, **12**, 2774-2780.

16. R.-h. Yuan, Y. He, W. He, M. Ni and M. K. H. Leung, *Appl. Energ.*, 2019, **251**, 113406.

17. L. Chen, Y. Zhang, X. Liu, L. Long, S. Wang, X. Xu, M. Liu, W. Yang and J. Jia, *Carbon*, 2019, **151**, 10-17.

18. J.-T. Ren, Y.-S. Wang, L. Chen, L.-J. Gao, W.-W. Tian and Z.-Y. Yuan, *Chem. Eng. J.*, 2020, **389**, 124408.

19. L. Gao, M. Zhang, H. Zhang and Z. Zhang, *J. Power Sources*, 2020, **450**, 227577.

20. W. Liu, B. Ren, W. Zhang, M. Zhang, G. Li, M. Xiao, J. Zhu, A. Yu, L. Ricardez-Sandoval and Z. Chen, *Small*, 2019, **15**, e1903610.

21. J. Wang, X. Zheng, Y. Cao, L. Li, C. Zhong, Y. Deng, X. Han and W. Hu, *ACS Appl. Mater. Interfaces*, 2020, **12**, 8115-8123.

22. L. Feng, R. Ding, Y. Chen, J. Wang and L. Xu, *J. Power Sources*, 2020, **452**, 227837.